# Ultra-High-Temperature Ceramic Matrix Composites in Hybrid Rocket Propulsion Environment

Stefano Mungiguerra [1], Giuseppe D. Di Martino [2], Raffaele Savino[3]
*Università di Napoli "Federico II", 80125 Napoli, Italy*

Luca Zoli[4], Diletta Sciti[5]
*National Research Council, Institute of Science and Technology for Ceramics, 48018 Faenza, Italy*

Miguel A. Lagos[6]
*TECNALIA, E-20009 Donostia - San Sebastian, Spain*

**This paper is focused on the experimental characterization of a new class of Ultra-High-Temperature Ceramic Matrix Composites for near-zero erosion rocket nozzles. A novel test set-up has been developed to the purpose of testing small-sized samples of material in free-jet configuration, exposing them to the supersonic exhaust plume of a 200N-class hybrid rocket nozzle, employing gaseous oxygen as oxidizer and High-Density PolyEthylene as fuel. The aim of the tests was to screen the best material candidates for the final application. Two increasingly demanding test conditions have been selected. Four samples were manufactured, one based on chopped carbon fibers in a $Ti_3SiC_2$ matrix, and three based on $ZrB_2$-SiC matrix with continuous carbon fibers. Samples surface temperatures were monitored by two-color pyrometers and an infra-red thermo-camera. In two cases, sudden jumps of temperature were detected, up to over 2800 K, associated to considerable erosion, presumably related to poor mechanical resistance of the oxidized phases forming on the exposed surface. Computational Fluid Dynamics simulations were performed in order to characterize the test conditions and investigate the material thermal behavior.**

## I. Nomenclature

| | | | |
|---|---|---|---|
| $A_K$ | = chemical kinetic pre-exponential factor | p | = pressure, bar |
| C | = specific heat, J/kg·K | $\dot{q}$ | = heat flux, W/m$^2$ |
| $E_a$ | = activation energy, J/mol | $R$ | = universal gas constant, J/K·mol |
| K | = reaction rate coefficient | T | = temperature, K |
| n | = normal-to-surface coordinate, m | t | = time, s |

**Subscripts**

| | |
|---|---|
| g | = gas |
| int | = interface |
| rad | = radiation |
| s | = solid |

**Greek Symbols**

| | |
|---|---|
| $\beta$ | = Temperature exponent |
| $\varepsilon$ | = Emissivity |
| ρ | = density, kg/m$^3$ |
| σ | = Stefan-Boltzmann constant, W/m$^2$·K$^4$ |

[1] Ph.D. student, Dipartimento di Ingegneria Industriale, Aerospace Division, P.le Tecchio 80, Napoli, Italy
[2] Ph.D. student, Dipartimento di Ingegneria Industriale, Aerospace Division, P.le Tecchio 80, Napoli, Italy
[3] Professor, Dipartimento di Ingegneria Industriale, Aerospace Division, P.le Tecchio 80, Napoli, Italy
[4] Researcher, Institute of Science and Technology for Ceramics, Via Granarolo 64, Faenza, Italy
[5] Researcher, Institute of Science and Technology for Ceramics, Via Granarolo 64, Faenza, Italy
[6] Senior Researcher, Industry and transport division, Mikeletegi Pasealekua, 2, San Sebastian, Spain

## II. Introduction

Challenges for solid and hybrid rocket technologies include the optimization of thermal insulations and the design and fabrication of non-eroding firing thrusters able to survive severe thermal-structural and thermal-chemical combustion environments without cooling systems. The inner surface of the exhaust nozzle, through which the propellant flow is accelerated to supersonic conditions, is very critical in this sense, as it is subjected to the highest shear stresses, pressure and heat fluxes in a chemically aggressive environment. These severe conditions usually lead to removal of surface material (ablation) due to heterogeneous reactions between oxidizing species in the hot gas and the solid wall. Because of the material erosion, there is an enlargement of the nozzle throat section and a consequent decrease of the rocket thrust, with detrimental effects over the motor operation. Thus, the requirement that dimensional stability of the nozzle throat should be maintained makes the selection of suitable rocket nozzle materials extremely hard.

The materials used for these applications include refractory metals, refractory metal carbides, graphite, ceramics and fiber-reinforced plastics [1, 2]. Certain classes of materials demonstrated superior performances under specific operating conditions but the choice depends on the specific application. For instance, fully densified refractory-metal nozzles generally are more resistant to erosion and thermal-stress cracking than the other materials. Graphite performs well with the least oxidizing propellant but is generally eroded severely [3, 4, 5].

In recent years, Ultra-High-Temperature Ceramic (UHTC) materials, including zirconium or hafnium diborides or carbides, are assuming an increasing importance in aerospace research because of their high temperature capabilities, with melting points above 3500 K, high temperature strength and oxidation resistance at service temperatures exceeding 2300 K. Some of these materials proved to be very interesting to develop aerospace components working in harsh environments [6, 7, 8]. The use of single-phase materials, without secondary phases, is not sufficient because they are characterized by low fracture toughness, low thermal shock resistance and lack of damage tolerance [9]. To improve their properties UHTCs composites with SiC or other Silicon based ceramics, in the form of particles, short fibers or whiskers have been developed with better tolerance and thermal shock resistance in aggressive chemical environments [10, 11]. Unfortunately, despite the very good oxidation resistance of small specimens, larger UHTC components frequently exhibit poor reliability and are subject to failures in high enthalpy flows. Based on these results, the current research activities are oriented towards Ultra-High-Temperature Ceramic Matrix Composites (UHTCMC) materials based on C or SiC continuous fibers in UHTC matrices that represent the next step to introduce significant improvements in comparison to the state-of-art materials for aerospace applications [12, 13].

In this framework, University of Naples "Federico II" (UNINA), the Institute of Science and Technology for Ceramics (ISTEC) and the Spanish Research&Innovation Corporation TECNALIA are involved in the Horizon 2020 European C$^3$HARME research project, focused on a new class of UHTCMCs for near zero-erosion rocket nozzles. In particular, an extensive experimental characterization campaign is ongoing, based on an incremental approach, envisaging tests on prototypes of increasing complexity, from small button-like samples to complete sub-scaled De Laval nozzles [14].

In the present work, a major focus is given to the experimental activities aimed at screening the most suitable materials candidates for the final applications. A novel, dedicated test set-up was developed and successfully employed at UNINA Aerospace Propulsion Laboratory to expose different UHTCMC samples manufactured by ISTEC and TECNALIA to the supersonic exhaust jet of a 200N-class hybrid rocket nozzle. The propellants employed were gaseous oxygen as oxidizer and a cylindrical grain of solid High-Density PolyEthylene (HDPE) as fuel. Non-intrusive diagnostic equipment, including two-color pyrometers and an infrared thermocamera, has been employed to monitor the surface temperature of the samples, that reached values over 2800 K. The combination of combustion temperature over 3000 K, supersonic Mach number and stagnation pressures allowed reproducing realistic rocket nozzles operating conditions, in order to demonstrate the ability of the specimens to preserve their functional integrity in a relevant environment, hence supporting the selection of the most promising materials compositions. Post-test inspections were carried out to analyse the surface modifications occurred after the exposition to the aero-thermo-chemically aggressive combusting flow.

Finally, since the flow conditions generated inside hybrid rocket engines are extremely complex and not all the critical parameters can be measured experimentally, in order to support the experimental activities, numerical models have been defined, able to predict the thermo-fluid-dynamic flow field around the test articles and also the behavior of the materials prototypes. In this way, the characterization of the operating conditions has been obtained by a combined effort of experimental diagnostics and Computational Fluid Dynamics (CFD) simulations through interactive processes, providing a step-by-step improved understanding of the facility performance.

## III. Materials and methods

### A. Experimental set-up

The test rig is a versatile set up primarily designed for testing hybrid rocket engines of several sizes [15]. It is equipped with a test bench and a general-purpose acquisition system, which allow evaluating propellant performance and combustion stability [16], testing of sub-components and/or complete power systems, nozzles [17], air intakes, catalytic devices [18], burners, ignition and cooling systems [19, 20]. For the current research activities, a novel, dedicated test set-up was developed to expose different UHTCMC samples to the supersonic exhaust jet of a 200N-class hybrid rocket nozzle, in order to characterize the material behavior and select the most suitable candidates for manufacturing near-zero erosion rocket nozzles.

The schematics of the rocket employed in this work is depicted in Fig. 1, which also shows the UHTCMC sample (in blue) behind the rocket nozzle.

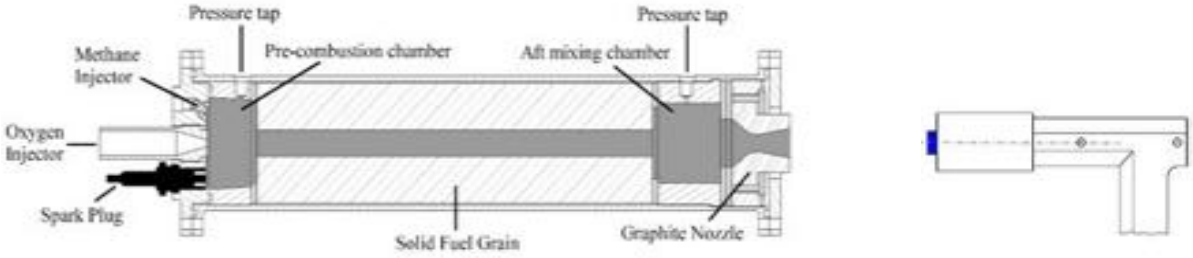


**Fig. 1. Layout of 200 N-class hybrid rocket engine, including the setup for UHTCMC free-jet testing.**

A detailed description of the laboratory and of the experimental facilities can be found in Ref. [15]. The tests presented in the following sections were performed with a converging nozzle injector, whose exit-section diameter is 6 mm, which delivered oxygen in single-port cylindrical fuel grains of HDPE. A graphite converging-diverging exhaust nozzle with an area ratio of 2.54, is employed to expand the combustion products up to supersonic speeds.

Oxidizer mass flow rate is controlled by means of a Tescom ER3000 pressure regulator, which controls an electropneumatic valve in order to reduce the pressure to the desired setpoint, upstream a chocked Venturi nozzle. The average fuel mass flow rate is estimated by means of grain mass measurements before and after the test (see Ref. [21]).

In the framework of the current research activities, the facility has been upgraded to allow performing tests on small, button-like samples, with maximum diameter of 17mm (Fig. 2).

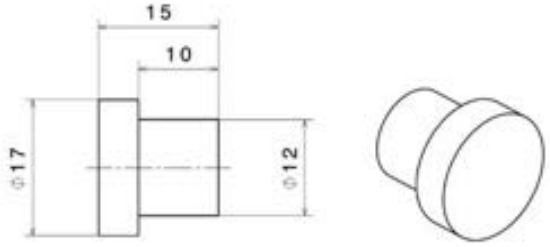


**Fig. 2. Nominal design of UHTCMC samples for free jet tests. Dimensions are in mm.**

The specimen is placed downstream the hybrid rocket engine, in order to be reached by the exhaust plume coming from the nozzle. The experimental set-up consists in a mechanical system connected to the test bench in order to support and keep the specimen aligned with the motor axis. This system is designed to place the test article at the desired distance to the nozzle exit. In the present test campaign, a distance of 15 cm was selected.

Fig. 3 shows the experimental set-up, including the non-intrusive diagnostic equipment employed for the real-time evaluation of the sample surface temperature. In particular, the surface temperature of the samples can be continuously measured (±1% instrumental accuracy) by digital two-color pyrometers (Infratherm ISQ5 and IGAR6, Impac

Electronic GmbH, Germany) at an acquisition rate of 100 Hz. In addition, the infrared response of the specimen during the free-jet testing can be obtained by means of an infrared (IR) thermo-camera (TC, Pyroview 512N, DIAS Infrared GmbH, Germany). The two-color ISQ5 pyrometer exploits two overlapping infrared wavelength bands at 0.7–1.15 μm and 0.97–1.15 μm to measure the temperature from 1273 K up to 3273 K. The IGAR6 pyrometer operates in the bands 1.5-1.6 μm and 2.0-2.5 μm to return the sample temperature in the range 523-2273 K. The two pyrometers gave perfectly equivalent responses, so only the temperature profiles measured by ISQ5 are herein reported. The pyrometers mode can be set in order to give back the peak value of the temperature field detected inside the measurement area, consisting in a round spot of 3.3 mm in diameter. In addition, the so-called "two-color mode" provides an output value independent on the (directional) spectral emittance. It is generally assumed that the observed surface behaves as a gray body over the operating temperature range. Surface chemical reactions occurring during test can be responsible for changes in emittance versus testing time. On one hand, the two-color pyrometers overcome this problem measuring the true temperature. On the other hand, the IR-TC detects the spectral radiance coming out from the heated sample along the infrared band wavelengths of 0.8-1.1 μm. The surface temperature distribution can be calculated assuming constant emissivity along the monitored surfaces of the samples and taking into account the axial symmetry of the specimens. Once the local temperature is measured thanks to the pyrometer at the measurement spot, that value is input to determine the spectral emittance in the range of the IR-TC, and finally the surface temperature distribution is evaluated.


**Fig. 3. Set-up for free-jet test. The area within the red circle in the left picture is zoomed in the right picture.**

### B. UHTCMC samples

Four UHTCMC samples were manufactured. All of them were based on a UHTC matrix with Carbon fibers ($C_f$).

One sample had a $Ti_3SiC_2$ matrix with short (chopped) carbon fibers, uniformly dispersed into the matrix, and it is referred as TSC-SF. Three samples were based on $ZrB_2$ as major component and SiC as a minority phase, and long continuous fibers, with a 0°/90° plies architecture, in a volume ratio of around 50%. They will be referred herein as ZBSC-LF-1, ZBSC-LF-2 and ZBSC-LF-3.

Samples ZBSC-LF-1 and TSC-SF have been tested at the same flow conditions in order to compare the performances of very different materials, based on different ceramic matrix and different fiber architectures.

Samples ZBSC-LF-2 and ZBSC-LF-3 are very similar in composition and fiber architecture and have been characterized at the most severe aero-propulsion conditions in order to select the most promising materials for extreme environment.

Samples external surfaces were observed before and after the test by a Digital Microscope KH-8700 (HIROX-USA, Inc., United States), employing a MX(G) 5040SZ optical lens with 50-400x magnification factor, which provided also measurements of diameters and thicknesses. These were also measured by a digital caliper (0.01 mm accuracy).

Initial and final masses of the samples were measured by a precision balance (1 mg accuracy) to evaluate the erosion rates.

### C. Numerical models

In order to provide an improved understanding of test conditions and materials thermal behavior, numerical simulations are performed. Herein, the physical and numerical models employed to characterize the operating conditions, the thermo-fluid dynamic behavior of the combusting flow field and the unsteady heating of the test articles will be described.

First, the conditions inside the hybrid rocket combustion chamber and throughout the exhaust nozzle are evaluated by means of the one-dimensional CEA chemical equilibrium code developed by NASA [22], under the hypothesis of frozen chemical equilibrium in the divergent part of the nozzle. Required inputs are the choice of the propellants, the chamber pressure, the Oxidizer-to-Fuel ratio and the nozzle area ratio. Pressure is directly measured during engine operation. Oxidizer-to-Fuel ratio is derived from measurements of average propellants mass flow rates. Consistency of results with experimental conditions is verified by matching the actual mass flow rate with that derived by software calculations (given by the product of the total mass flux times the area in the corresponding section, e.g. at nozzle throat).

Outputs of the simulations are the average values of the thermo-fluid-dynamic conditions and the gas mixture chemical composition in the combustion chamber and at nozzle exit section. The latter can be used as inputs for the Computational Fluid Dynamic (CFD) simulation of the flow field around the test article, which is then coupled with the thermal field inside the sample. To this purpose the Reynolds-Averaged Navier-Stokes (RANS) equations for single-phase multicomponent turbulent reacting flows are solved with a control-volume-based technique and a density-based algorithm [23], employing the Shear Stress Transport (SST) $k$–$\omega$ model as turbulence closure [24]. A detailed analysis of thermo-chemical evolution of gas mixture is performed, in order to have an accurate prediction of heat transfer at solid walls. The transport equations for the main combustion products ($O_2$, $C_2H_4$, $H_2O$, $CO_2$, CO, $H_2$, H, O, OH are the species considered in the current model, together with the non-reacting $N_2$) are solved, and the Eddy Dissipation Concept (EDC) model [25] is employed for the combustion mechanism, which accounts for detailed chemical reaction rates in turbulent flows. Consequently, the Arrhenius rate $K$ for each reaction is calculated as

$$K = A_K T^{\beta} \exp\left(-\frac{E_a}{RT}\right) \tag{1}$$

where the constants have been taken from Ref. [26] and are reported in Table 1.

The Discrete Ordinates model [27] for the radiation is included in the numerical modelling.

| No. | Reaction[a] | $A_K$[b] | $\beta$ | $E_a$[b] |
|---|---|---|---|---|
| 1 | $C_2H_4 + O_2 \rightleftarrows 2CO + 2H_2$ | 1.80e+14 | 0.0 | 35500 |
| 2 | $CO + O \rightleftarrows CO_2 + M$ | 5.30e+13 | 0.0 | -4540 |
| 3 | $CO + OH \rightleftarrows CO_2 + M$ | 4.40e+06 | 1.5 | -740 |
| 4 | $H_2 + O_2 \rightleftarrows OH + OH$ | 1.70e+13 | 0.0 | 48000 |
| 5 | $H + O_2 \rightleftarrows OH + O$ | 2.60e+14 | 0.0 | 16800 |
| 6 | $OH + H_2 \rightleftarrows H_2O + H$ | 2.20e+13 | 0.0 | 5150 |
| 7 | $O + H_2 \rightleftarrows OH + H$ | 1.80e+10 | 1.0 | 8900 |
| 8 | $OH + OH \rightleftarrows H_2O + O$ | 6.30e+13 | 0.0 | 1090 |
| 9 | $H + H \rightleftarrows H_2 + M$ | 6.40e+17 | -1.0 | 0 |
| 10 | $H + OH \rightleftarrows H_2O + M$ | 2.2e+22 | -2.0 | 0 |

[a]Third-body efficiencies for all thermolecular reactions are 2.5 for $M = H_2$, 16.0 for $M = H_2O$, and 1.0 for all other $M$.

[b]Units are in seconds, moles, cubic centimeters, calories and Kelvin.

**Table 1. $C_2H_4$ – $O_2$ reaction system.**

The computational grid used for the simulation of the free reacting jet exiting from the nozzle is shown in Fig. 4. Also the solid regions for the thermal analysis of the test articles and components are included. A pressure inlet boundary condition is set on the surface representative of the nozzle exit section, imposing the total pressure and the total temperature corresponding to the operating chamber pressure and temperature in the rocket and the static pressure and the chemical composition at the exit of the nozzle. The ambient pressure is set on the other external boundaries of the computational domain.

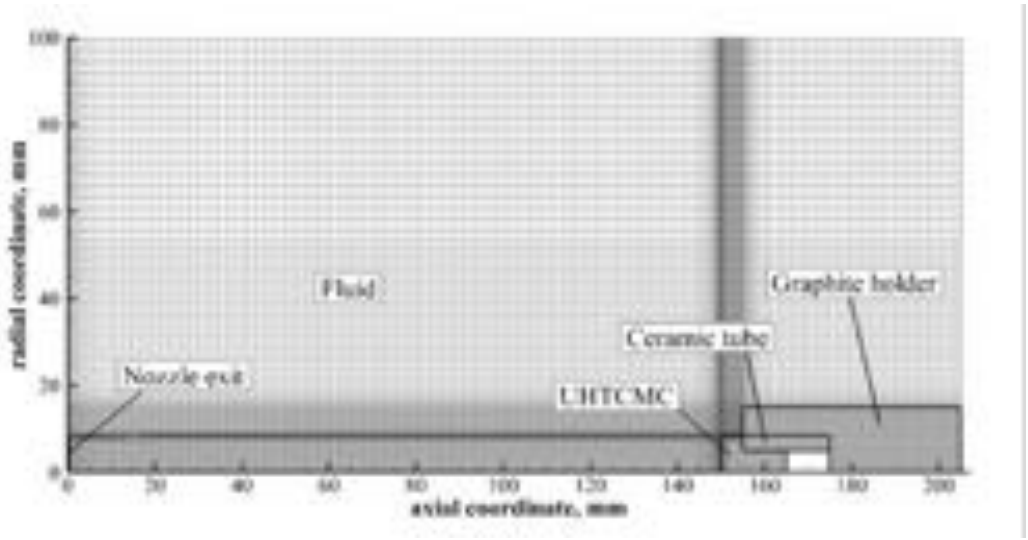


**Fig. 4. Computational grid for the simulation of the free reacting jet exiting from the rocket nozzle and the thermal field of the test sample exposed to the exhaust plume**

The last step of the numerical simulations is related to the thermal analysis of the samples tested.

In particular, the time-dependent temperature field inside the sample and its supporting elements can be computed solving the energy equation

$$(\rho C)_s \frac{\partial T}{\partial t} = k_s \nabla^2 T \tag{2}$$

where $\rho_s$, $C_s$ and $k_s$ are the solid density, specific heat and thermal conductivity, respectively.

The distribution of the thermo-fluid dynamic quantities and the chemical compositions in the fluid area near the solid material, and subsequently the convective heat flux, are influenced by the temperature on the exposed surface of the sample. For these reasons, for an accurate approach the interaction between the fluid and the materials has to be considered. Hence, the thermal coupling condition is set on the interfaces between fluid and solid domains, that is temperature and heat flux continuities:

$$T_{f,int} = T_{s,int} \tag{3}$$

$$k_f \left.\frac{\partial T}{\partial n}\right|_{f,int} + \dot{q}_{rad,in} = k_s \left.\frac{\partial T}{\partial n}\right|_{s,int} + \dot{q}_{rad,out} \tag{4}$$

where $n$ is the normal direction of the interface, the subscript $f$ represents fluid, $\dot{q}_{rad,in}$ is the radiative heat flux entering the solid domain, $\dot{q}_{rad,out} = \varepsilon\sigma T^4$ is the radiative heat flux emitted by the solid surface.

## IV. Test conditions and experimental results

### A. Test conditions

Two different test conditions, which differ for the oxidizer mass flow rates, have been selected, to evaluate the materials performance in different aero-thermo-chemical environments. All tests had a nominal duration of 10 s. Cylindrical 220mm-long HDPE grains were employed as fuel and gaseous oxygen as oxidizer. During the tests, an average port diameter of around 25 mm was reached. Table 2 summarizes the main parameters of the test conditions.

Measured O/F ratios and chamber pressures are averaged over test time and over different tests. All the quantities that are not directly measurable were estimated by the one-dimensional tool described in Section III.C. One can notice that Test Condition 2 is more severe due essentially to the higher pressure and a more oxidizing environment, as deductible from the higher concentration of oxygen at nozzle exit. Further details about the effects of the test conditions on the material behavior will be given in the Section dedicated to the numerical simulations.

| | Test condition 1 | Test condition 2 |
|---|---|---|
| Oxidizer mass flow rate [g/s] | 25 | 30 |
| Measured Average Oxidizer-to-Fuel ratio | 5.3 | 5.7 |
| Measured Average chamber pressure [bar] | 5.5 | 6.5 |
| Estimated Combustion temperature [K] | ~ 3200 | ~ 3200 |
| Estimated Nozzle Exit Pressure [bar] | 0.45 | 0.54 |
| Estimated Nozzle Exit Mach Number | 2.25 | 2.25 |
| Estimated Nozzle Exit Total mass flux [kg/m$^2$-s] | 137 | 163 |
| Estimated Nozzle Exit $CO_2$ mass fraction | 0.36 | 0.35 |
| Estimated Nozzle Exit $H_2O$ mass fraction | 0.17 | 0.16 |
| Estimated Nozzle Exit $O_2$ mass fraction | 0.30 | 0.34 |

**Table 2. Summary of test conditions.**

### B. Experimental results

*1. Experiments in Test Condition 1*

First, two tests were carried out in Test Condition 1 (Table 2), in order to compare the response of material with very different compositions. A long fibers $ZrB_2$-SiC-based sample (ZBSC-LF-1) and the chopped fibers $Ti_3SiC_2$-based sample (TSC-SF) were exposed to the exhaust plume of the hybrid rocket, injecting a gaseous oxygen mass flow rate of 25 g/s. The time profile of the maximum surface temperature for the two samples is shown in Fig. 5. The thermal histories practically overlap for the first 4-5 s, then, when T approaches 1900 K, the TSC-SF sample experiences a sudden rise in temperature, which at the end of the test exceeds 2800 K.

The sudden temperature jump was associated to a change in the shape of the flame surrounding the sample, as clearly shown by comparison between Fig. 6 and Fig. 7, which depict images taken during test on ZBSC-LF-1 and TSC-SF respectively, at the beginning and at the end of the test. In particular, starting from the instant corresponding to the jump, a very bright halo developed in front of the TSC-SF sample, from which a considerable amount of material was removed, probably due to the extremely high shear stresses. This resulted in a consistent erosion, estimated to be 0.204 mm/s, based on mass measurements. On the contrary, the stable behavior exhibited by sample ZBSC-LF-1 was associated to a near-zero erosion rate ($5*10^{-4}$ mm/s).

Fig. 8 shows four pictures taken by the infrared thermo-camera before and after the temperature jump occurred on sample TSC-SF. Immediately before the jump, the temperature on the front surface of the sample was relatively

uniform. The temperature jump corresponds to a steep increase in temperature by almost 300 K in 0.5 s, localized in the central region of the surface. This also appears in Fig. 9, showing the temperature radial profiles on the sample surface at different time instants. As will be verified by numerical simulations, this is the area where the heat flux is most intense and the concentration of molecular oxygen is expected to be higher, so the jump might be associated to triggering, at high temperature, of chemical reactions involving the species contained in the ceramic matrix and/or the carbon fibers; the exothermic release of gaseous products might also justify the change in shape and brighteness of the flame surrounding the sample, which was also detected by the thermo-camera, as noticeable in the last two pictures of Fig. 8.

Finally, Fig. 10 and Fig. 11 show pictures of the two samples before (top) and after (bottom) test, taken by a CCD camera and the optical microscrope described in Section III.B. In the pictures taken before the test, the continuous fiber structure of the sample is observable. It is clear that the $ZrB_2$-SiC-based sample preserved its original shape with no erosion. However, the microscopic observation of the surface revealed the presence of a thin, irregular white layer, after the test, presumably associated to oxidation of zirconium contained in the sample matrix. The Titanium Silicocarbide-based sample, on the contrary, eroded significantly, and the exposed surface appears to be almost completely oxidized.

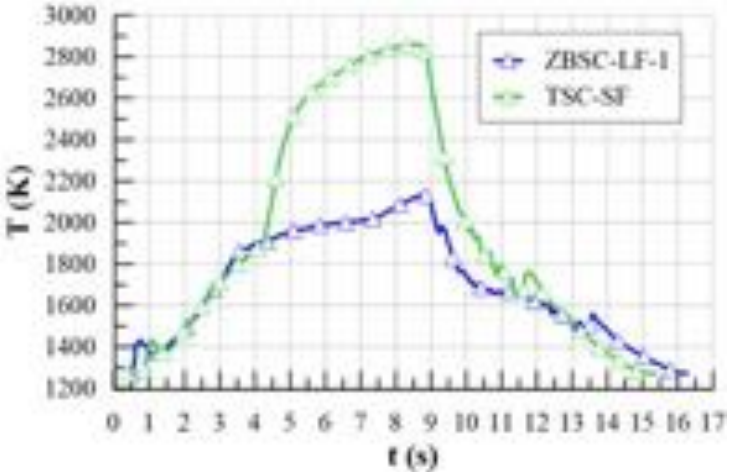


**Fig. 5. Thermal histories of the two samples tested in Test Condition 1.**

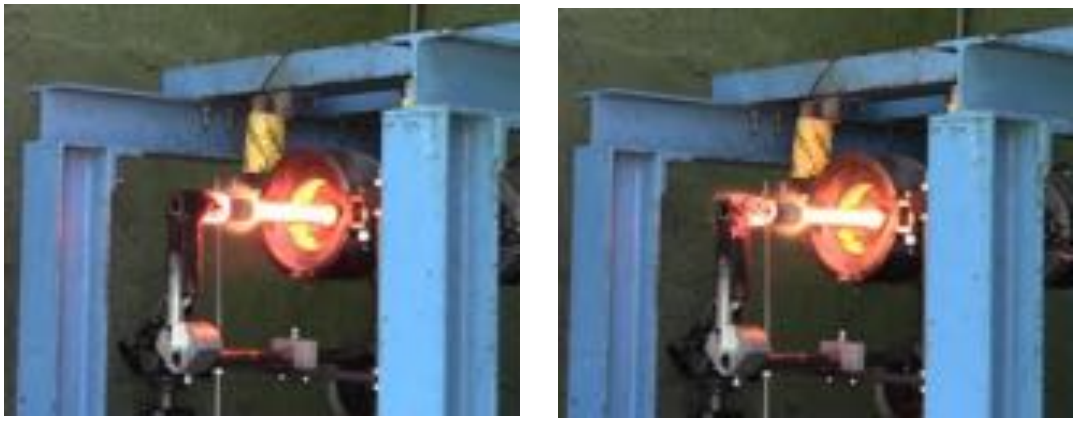

**Fig. 6. Pictures of test on ZBSC-LF-1 sample, at beginning (left) and end (right) of the test (Test Condition 1).**

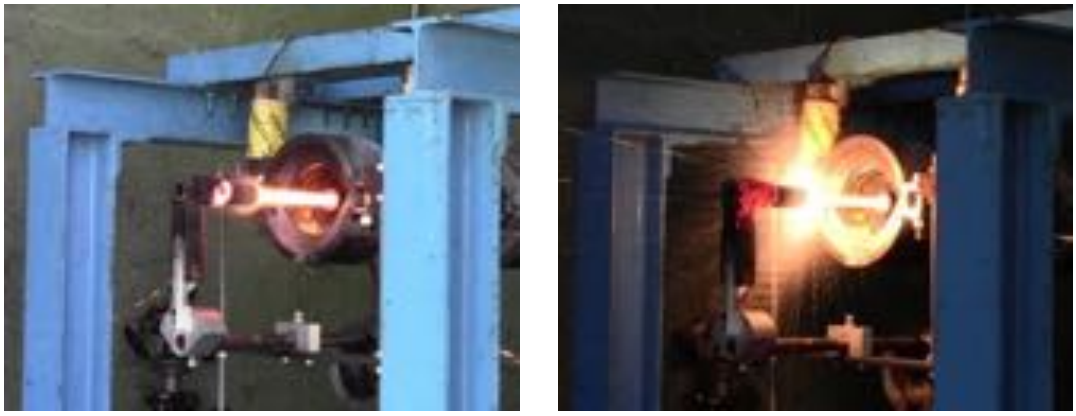

**Fig. 7. Pictures of test on TSC-SF sample, at beginning (left) and end (right) of the test (Test Condition 1).**

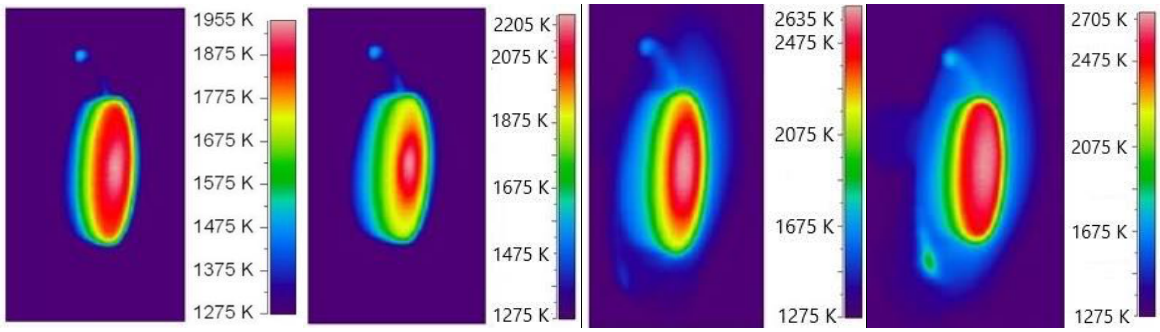


(a) t = 4.4 s (b) t = 4.9 s (c) t = 5.4 s (d) t = 5.9 s

**Fig. 8. IR thermal images of TSC-SF sample, taken every 0.5 s, starting from immediately before the temperature jump.**

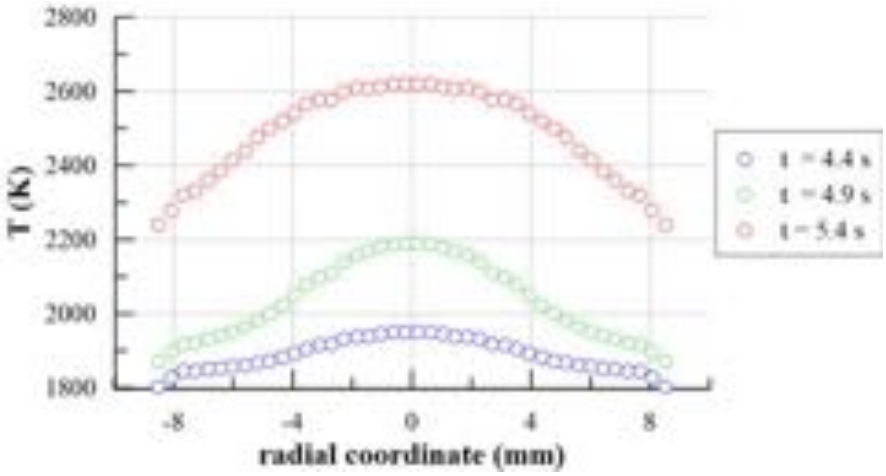


**Fig. 9. Temperature radial profiles, measured by the thermo-camera, on sample TSC-SF front surface at different time instants, around the temperature jump.**

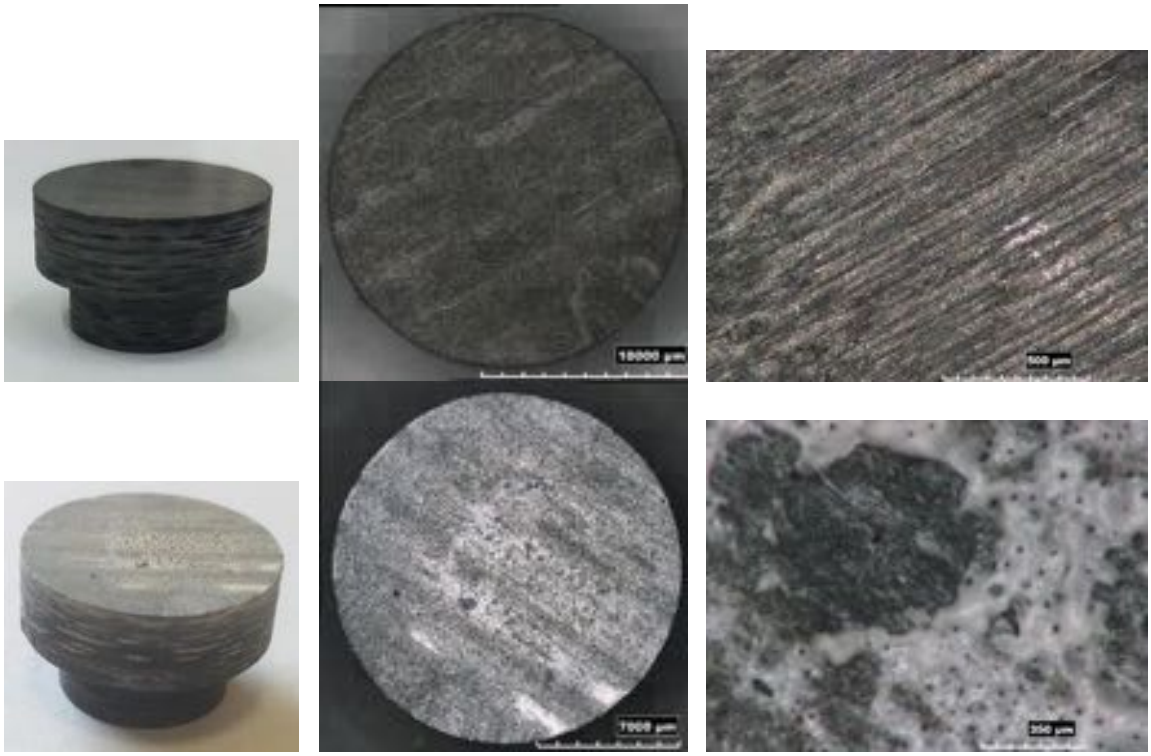

**Fig. 10. Pictures of sample ZBSC-LF-1 before (top) and after (bottom) the test.**

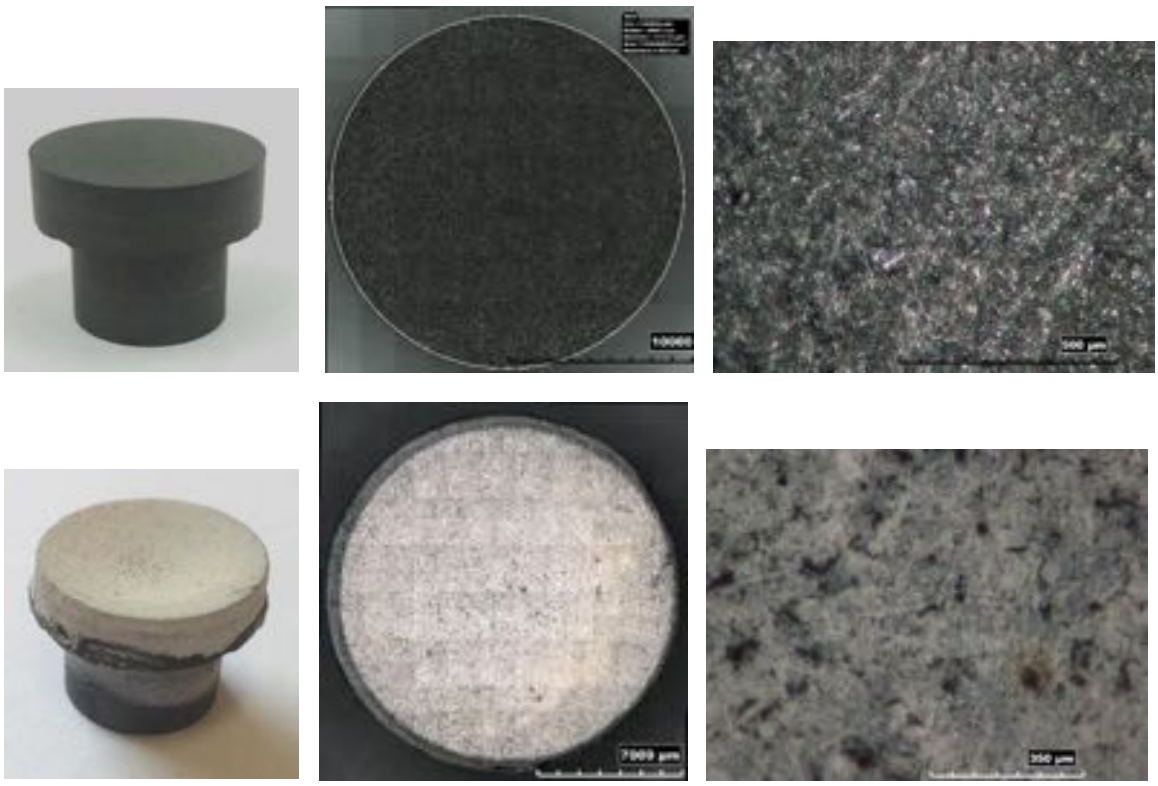

**Fig. 11. Pictures of sample TSC-SF before (top) and after (bottom) the test.**

*2. Experiments in Test Condition 2*

Since the sample based on $Ti_3SiC_2$ matrix did not exhibit a satisfactory erosion resistance, in the less demanding condition, only $ZrB_2$-based samples were considered for testing in Test Condition 2. Fig. 12 shows the time history of the maximum temperature reached by samples ZBSC-LF-2 and ZBSC-LF-3. Although the test conditions were the same, the final temperatures reached by the samples differed by over 400 K. In fact, after 4-5 s, the temperature of ZBSC-LF-2 started rising more rapidly, and a phenomenon similar to the jump observed on TSC-SF sample occurred. Also in this case, the extremely high temperatures reached (over 2800 K) were associated to a considerable sample erosion (0.154 mm/s), and solid fragments wiped off the sample surface by the oncoming supersonic flow are visible in Fig. 13, showing a comparison between beginning and end of test on sample ZBSC-LF-2. On the contrary, sample ZBSC-LF-3 preserved stable mass and dimensions.

Fig. 14(a) and (b) show respectively pictures of samples ZBSC-LF-2 and ZBSC-LF-3 before (top) and after (bottom) the test. Both the samples appear to be oxidized after exposition to the supersonic flame, but, whereas the oxide layer of ZBSC-LF-3 survived the mechanical loads, preserving structural integrity, the oxidized part of ZBSC-LF-2 had too poor mechanical properties to withstand the shear stresses and was consistently removed, in particular in the central area of the surface. Once again, the images recorded by the thermo-camera, shown in Fig. 15, and the temperature radial profiles, displayed in Fig. 16, verify that the temperature starts rising suddenly in a localized region in the center of the surface. The porosity left by depletion of carbon fibers and the characteristic low thermal conductivity of oxidized phases such as $ZrO_2$ [28, 29], together with the peaked distribution of heat flux along the surface, might have favored the steep increase in temperature in the central area, therefore triggering the considerable thermo-mechanical erosion.

A plausible interpretation for the better resistance of sample ZBSC-LF-3 could be found in the optimized manufacturing process, which allowed for a more strict control on porosity level and mechanical properties. Further post-test analysis carried out by Scanning Electron Microscopy (SEM) of the samples cross-sections will allow comparing both the unoxidized bulk materials and the oxidized phases to provide a deeper comprehension of the material behavior.

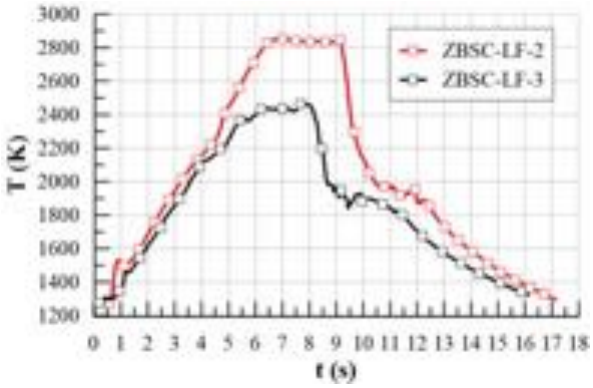


**Fig. 12. Thermal histories of the two samples tested in Test Condition 2.**

**Fig. 13. Pictures of test on ZBSC-LF-2 sample, before (left) and after (right) the temperature jump (Test condition 2).**

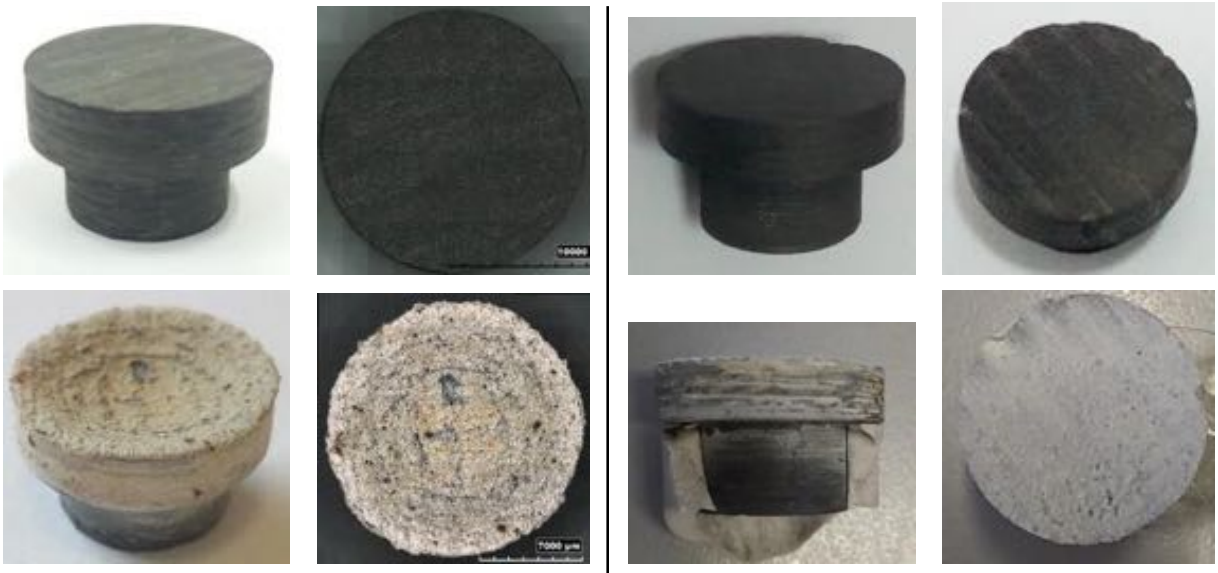

(e) ZBSC-LF-2 (f) ZBSC-LF-3

**Fig. 14. Pictures of samples (a) ZBSC-LF-2 and (b) ZBSC-LF-3 before (top) and after (bottom) the test.**

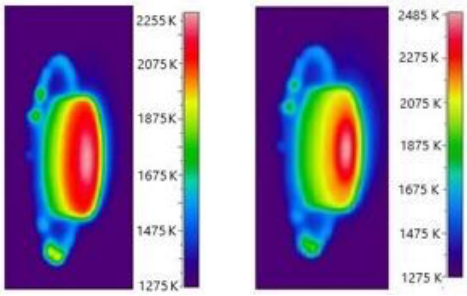


**Fig. 15. IR Thermal images of sample ZBSC-LF-2 before (left) and after (right) the abrupt temperature rise occurred around t = 4.5 s.**

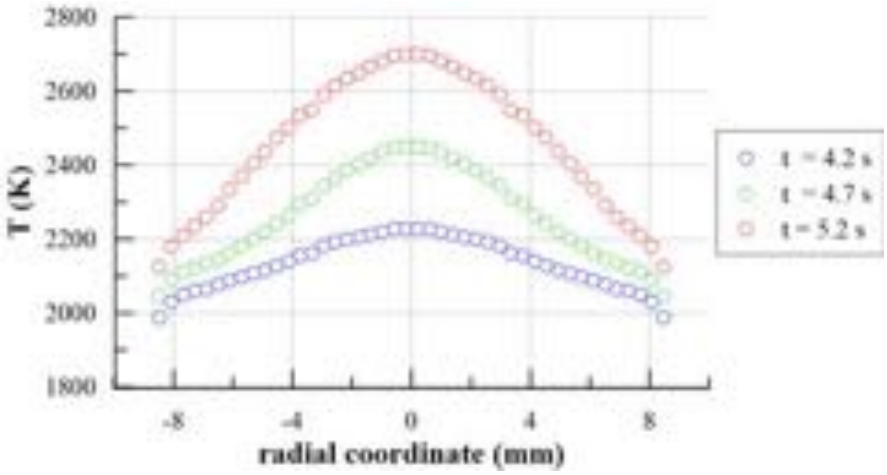


**Fig. 16. Temperature radial profiles, measured by the thermo-camera, on sample ZBSC-LF-2 front surface at different time instants, around the temperature jump.**

## V. Numerical simulations

Numerical simulations are useful to provide a better understanding of the test conditions and propose interpretations for the experimental results. The models described in Section III.C were employed to predict, by CFD simulations, the thermo-fluid-dynamic conditions and the chemical composition in the exhaust plume of the nozzle.

Fig. 17 and following show the distributions of temperature, pressure and molecular oxygen mass fraction in the flow field, for both Test Conditions 1 and 2 (for a better comparison, the contours of the same quantities are plotted in the same scale for the two conditions). In particular, comparison between Fig. 17(a) and (b) verifies that the two test conditions do not differ significantly in terms of temperature distribution, as expectable due to the similar values of combustion chamber temperatures evaluated by means of the chemical equilibrium software. On the contrary, major differences are noticeable in the static pressure field, displayed in Fig. 18(a) and (b) for Test Conditions 1 and 2, respectively. Downstream a sequence of shock/expansion oblique waves, the peak static pressure at sample locations is slightly higher than 2.5 bar in Test Condition 1, and almost 4 bar in Test Condition 2. Furthermore, Fig. 19 shows the distribution of $O_2$ mass fraction, whose average value at sample location is 0.26 and 0.31, for Test conditions 1 and 2 respectively.

The thermo-fluid-dynamic and chemical flow fields produce the cold-wall heat flux profiles shown in Fig. 20, which differ, in the two Test Conditions, by 4 MW/m$^2$ for the peak value and by more than 2 MW/m$^2$ on average. It is possible to see that the heat flux in both cases is higher on the symmetry axis, which is the location where the temperature jump discussed in Section IV first occurs. One should moreover remark that, in the present computations, a one-dimensional model was employed for calculation of the conditions at nozze exit, which gave the average value of the oxygen mass fraction at nozzle exit. A more realistic distribution of the oxygen concentration could be predicted by the CFD solution of the fluid flow inside the combustion chamber and nozzle of the hybrid rocket, as presented in [30] for test conditions similar to the present ones. Results are compared in Fig. 21, demonstrating that the oxygen mass fraction is higher on the symmetry axis, due to the anular flame structure in the combustion chamber, which suggests the jump might be associated with triggering of material oxidation, starting in the central area of the sample surface. Future developments of the models will include the possibility to take into account the detailed description the flow field along the rocket nozzle as input for the free-jet configuration simulations.

Table 3 summarizes the main thermo-fluid-dynamic and chemical conditions at sample location.

| | Test condition 1 | Test condition 2 |
|---|---|---|
| Stagnation point pressure [bar] | 2.6 | 3.8 |
| Average $CO_2$ mass fraction | 0.27 | 0.29 |
| Average $H_2O$ mass fraction | 0.11 | 0.12 |
| Average $O_2$ mass fraction | 0.26 | 0.31 |
| Average Cold-wall surface heat flux [MW/m$^2$] | 10.8 | 12.9 |

**Table 3. Summary of conditions at sample location.**

Finally, the flow field solution has been coupled to the thermal analysis of the sample, assuming as a reference test case that on specimen ZBSC-LF-1, which exhibited both stable dimensions and almost null oxidation. The density of the sample was set to 4300 kg/m$^3$, based on mass and volume measurements. The specific heat was set to 1100 J/(kg·K), according to a rule of mixture also employed in [10] for the numerical simulation of the thermal behavior of a nozzle-throat insert with a similar composition. The thermal conductivity was set to 20 W/(m·K) and the surface emissivity was 0.85. Fig. 21 shows the comparison between experimental and numerical results in terms of maximum sample temperature, verifying the good capability of the model to predict the unsteady thermal behavior of the materials. Moreover, the blue line displays the time profile of the average surface heat flux on the front face of the sample, which decreases from the initial value of 10.8 MW/m$^2$ to almost 2 MW/m$^2$ when the sample approaches the steady state.

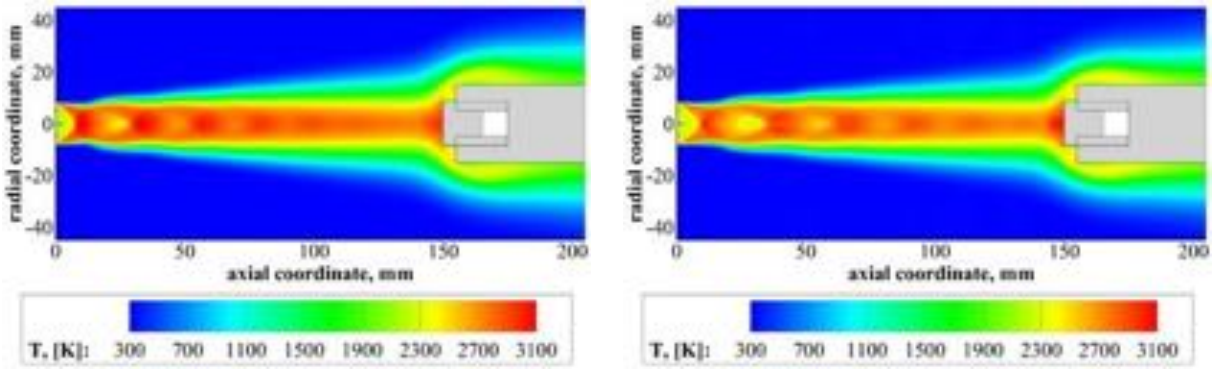


(a) (b)

**Fig. 17. Temperature distribution around the sample (a) for Test Conditon 1 and (b) for Test Condition 2.**

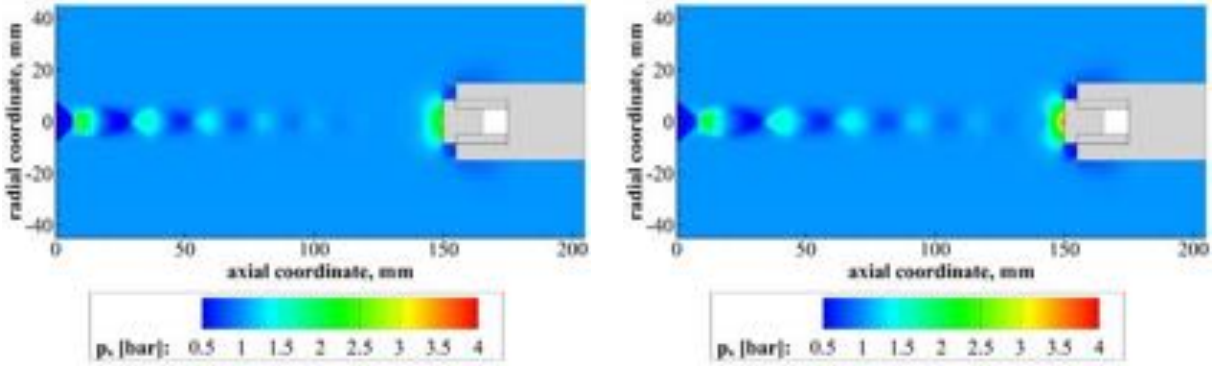


(a) (b)

**Fig. 18. Static pressure distribution around the sample (a) for Test Condition 1 and (b) for Test Condition 2.**

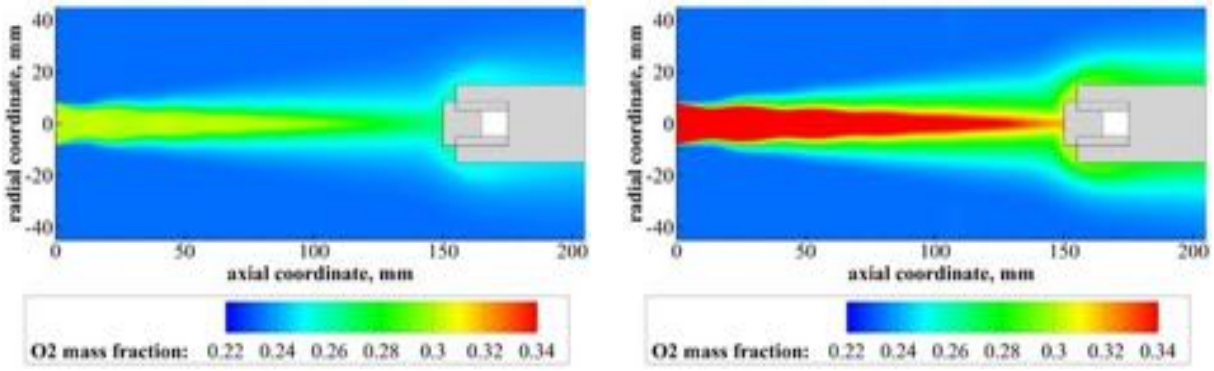


(a) (b)

**Fig. 19. $O_2$ mass fraction distribution around the sample (a) for Test Condition 1 and (b) for Test Condition 2.**

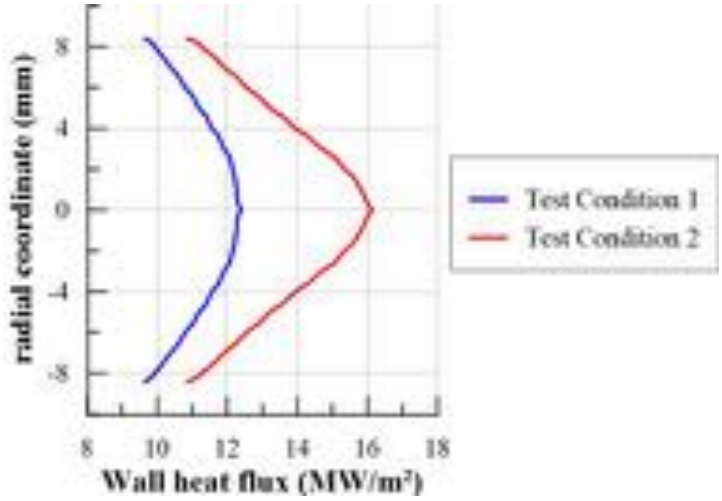


**Fig. 20. Cold-wall total surface heat flux on sample front surface.**

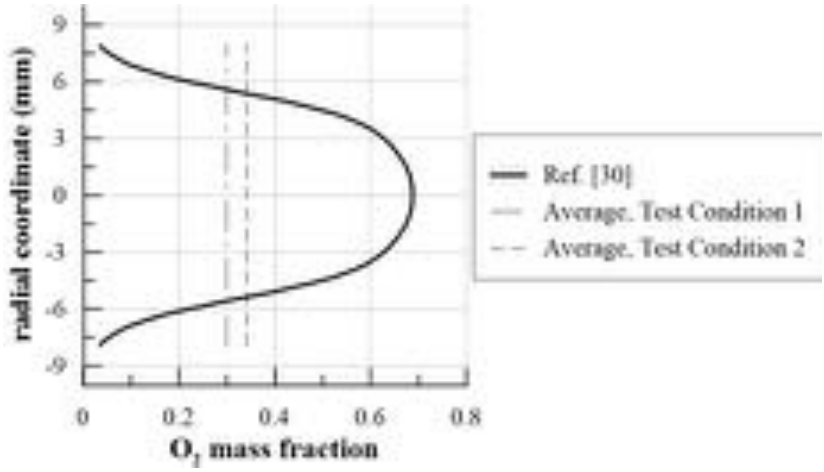


**Fig. 21. Comparison between profile of $O_2$ mass fraction computed by CFD in [30] and average values calculated with the present one-dimensional model.**

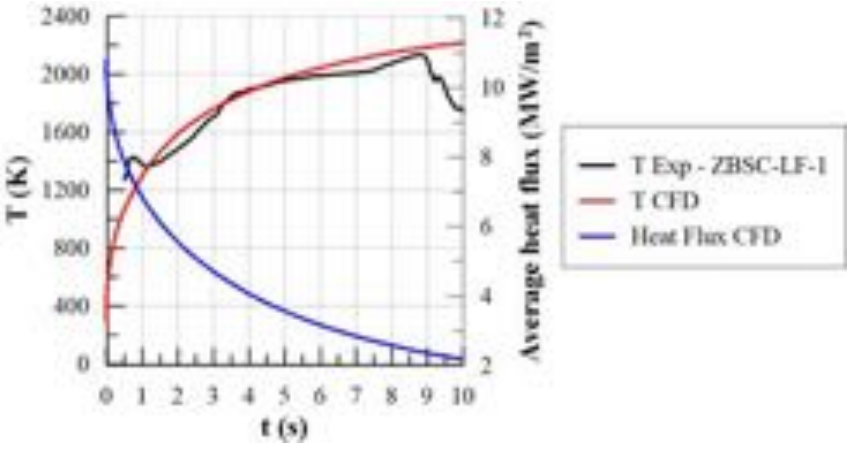


**Fig. 22. Comparison between numerical and experimental temperature profiles and numerical heat flux profile for Test condition 1.**

## VI. Conclusions and future developments

In this paper, the results of an experimental campaign aimed at the characterization of Ultra-High-Temperature Ceramic Matrix Composites for space propulsion applications have been presented. A dedicated test setup was developed to expose small-sized material samples to the supersonic exhaust plume coming from the nozzle of a 200N-class hybrid rocket engine, employing gaseous oxygen as oxidizer and High-Density PolyEthylene as solid fuel. The response of materials with different ceramic matrices and different carbon fibers architecture was investigated, in two increasingly demanding test conditions, which differed for the oxidizer mass flow rate. Surface temperatures were monitored by non-intrusive diagnostic equipment. In two cases, samples were consistently eroded and reached temperatures over 2800 K. Visual observations of the samples and Computational Fluid Dynamics simulations of the fluid flow suggested the sudden temperature jump associated to the erosion was related to triggering of oxidation mechanisms in the central area of the samples, were heat fluxes are expected to be most intense. Numerical simulations also allowed characterizing the test conditions in terms of temperature, pressure and chemical species distributions around the samples, and reconstructing the heat flux history in one of the test conditions, during the unsteady heating of the sample.

Future developments will certainly include more detailed material post-test characterization, e.g. based on Scanning Electron Microscopy (SEM) of the cross-sections of the materials, for an improved understading of chemical processes concurring to the experimental evidence. Moreover, the numerical models will be improved in order to provide a more accurate description of the flow field. Further tests, even at more severe test conditions, will be performed to complete the screening phase of the materials, in order to select the most promising candidates for manufacturing near-zero erosion nozzles.

## Acknowledgments

This project has received funding by the European Union's Horizon2020 research and innovation programme under the Grant Agreement 685594.

The authors wish to thank Prof. Claudio Leone and Dr. Silvio Genna (CIRTIBS Research Center) for technical support in realizing the microscopic pictures of the samples.

## References

[1] Hickman, R., Mc Kechnie, T., Agarwal, A., "Net shape fabrication of high temperature materials for rocket engine components," AIAA paper 2001-3435, 2001.

[2] Johnston, J. R., Signorelli, R. A., Freche, J. C., "Performances of rocket nozzle material with several solid propellants," NASA technical note 3428.3, 1966.

[3] Thakre, P., Yang, V., "Chemical erosion of carbon-carbon/graphite nozzles in solid-propellant rocket motors," *Journal of Propulsion and Power*, Vol. 24, No. 4, 2008, pp. 822-833.

[4] Murugan, J.P., Kurian, T., Jayaprakash, J., Jayachandran, T., "Design and Thermo-Structural Analysis of the Interface between Subscale Versions of Carbon-Carbon (C-C) Nozzle Divergent to Metallic flange hardware for a Ground Simulation Test", *68th International Astronautical Congress*, Adelaide, Australia, September 2017.

[5] Kamps, L., Hirai, S., Ahmimache, Y., Guan R., Nagata, H., "Investigation of Graphite Nozzle-Throat-Erosion in a Laboratory-Scale Hybrid Rocket Using GOX and HDPE," AIAA paper 2017-4736, Jul. 2017.

[6] Natali, M., Kenny, J. M., Torre, L., "Science and technology of polymeric ablative materials for thermal protection systems and propulsion devices: A review," *Progress in Materials Science*, Vol.84, 2016, pp. 192-275.

[7] Harrington, G. J. K., Hilmas, G. E., "Thermal conductivity of $ZrB_2$ and $HfB_2$", *Ultra-High Temperature Ceramics: Materials for Extreme Environment Applications*, edited by Fahrenholtz, W., Wuchina, E., Lee, W., Zhou, Y., 1st ed., John Wiley & Sons, Inc., 2014, pp. 197-235.

[8] Koo, J., Stretz, H., Weispfenning, J., Luo, Z., Wootan, W., "Nanocomposite rocket ablative materials: processing, microstructure, and performance," AIAA paper 2004-1996, Apr. 2004.

[9] Savino, R., Festa, G., Cecere, A., Pienti, L., Sciti, D. "Experimental Set Up for Characterization of Carbide-Based Materials in Propulsion Environment," *Journal of the European Ceramic Society*, Vol. 35, 2015, pp. 1715–1723.

[10] Sciti, D., Zoli, L., Silvestroni, L., Cecere, A., Martino, G.D., Savino, R. "Design, fabrication and high velocity oxy-fuel torch tests of a Cf-$ZrB_2$- fiber nozzle to evaluate its potential in rocket motors," *Materials and Design*, Vol. 109, 2016, pp. 709-717.

[11] Wang, Y., Chen, Z., Yu, S., "Ablation behaviour and mechanism of C/SiC Composites", *Journal of materials research and technology*, Vol. 5, 2016, pp. 170-18.

[12] Zoli, L., Sciti, D., "Efficacy of a ZrB2–SiC matrix in protecting C fibres from oxidation in novel UHTCMC materials," *Materials & Design*, Vol. 113, 2017, pp. 207-213.

[13] Zoli, L., Medri, V., Melandri, C., Sciti, D., "Continuous SiC fibers-ZrB2 composites," *Journal of the European Ceramic*

*Society*, Vol. 35, No. 16, 2015, pp. 4371-4376.
[14] Savino, R., Criscuolo, L., Di Martino, G.D., Mungiguerra, S., "Aero-thermo-chemical characterization of ultra-high-temperature ceramics for aerospace applications," *Journal of European Ceramic Society*, Dec. 2017.
[15] Carmicino, C., Scaramuzzino, F., Russo Sorge, A., "Trade-off Between Paraffin-Based and Aluminium-Loaded HTPB Fuels to Improve Performance of Hybrid Rocket fed with N2O," *Aerospace Science and Technology,* Vol. 37, 2014, pp. 81–92.
[16] Carmicino, C., "Acoustics, Vortex Shedding, and Low-Frequency Dynamics Interaction in an Unstable Hybrid Rocket," *Journal of Propulsion and Power*, Vol. 25, No. 6, 2009, pp. 1322–1335.
[17] Russo Sorge, A., Carmicino, C., Nocito, A., "Design of a Lab-scale Cooled Two-dimensional Plug Nozzle for Experimental Tests," AIAA paper 2002-4039, Jul. 2002.
[18] Bonifacio, S., Festa, G., Russo Sorge, A. "Novel Structured Catalysts for Hydrogen Peroxide Decomposition in Monopropellant and Hybrid Rockets," *Journal of Propulsion and Power*, Vol. 29, 2013, pp. 1130–1137.
[19] Savino, R., Festa, G., Cecere, A., Pienti, and Sciti, D. "Experimental Set Up for Characterization of Carbide-Based Materials in Propulsion Environment," *Journal of the European Ceramic Society*, Vol. 35, 2015, pp. 1715–1723.
[20] Galfetti, L., Nasuti, F., Pastrone, D., Russo, A.M., "An Italian Network to Improve Hybrid Rocket Performance: Strategy and Results," *Acta Astronautica,* Vol. 96, 2014, pp.246–260.
[21] Carmicino, C. and Russo Sorge, A., "Experimental Investigation into the Effect of Solid-Fuel Additives on Hybrid Rocket Performance," *Journal of Propulsion and Power*, Vol. 31, No. 2, 2015, pp. 699–713.
[22] Gordon, S., McBride, B.J., "Computer Program of Complex Chemical Equilibrium Compositions and Applications", NASA Reference Publication 1311, 1994.
[23]Chorin, A. J., "Numerical Solution of Navier-Stokes Equations," *Mathematics of Computation*, Vol. 22, 1968, pp. 745-762.
[24]Menter, F.R., "Two-Equation Eddy-Viscosity Turbulence Models for Engineering Applications," *AIAA Journal*, Vol. 32, No. 8, 1994, pp. 1598-1605.
[25] Magnussen, B.F., "On the Structure of Turbulence and a Generalized Eddy Dissipation Concept for Chemical Reaction in Turbulent Flow," In: *Nineteenth AIAA Meeting*, St. Louis,1981.
[26] Singh, D. J., and Jachimowski, C. J., "Quasigobal Reaction Model for Ethylene Combustion," *AIAA Journal*, Vol. 32, No. 1, 1994, pp. 213-216.
[27] Modest, M. F, "Radiative Heat Transfer 2nd Edition," Academic Press, New York, March 2003, Chapter 16.
[28] Deng, Z., Ferreira, J.M.F., Tanaka, Y., Isoda, Y., "Microstructure and thermal conductivity of porous $ZrO_2$ ceramics", *Acta Materialia*, Vol. 55, No. 11, 2007, pp. 3663-3669.
[29] Schlichting, K.W., Padture, N.P., Klemens, P.G., "Thermal conductivity of dense and porous yttria-stabilized zirconia", *Journal of Material Science*, Vol. 36, 2001, pp. 3003-3010.
[30] Di Martino, G.D., Mungiguerra, S., Carmicino, C., Savino, R., "Computational Fluid-dynamic Simulations of Hybrid Rocket Internal Flow Including Discharge Nozzle", *53rd AIAA/SAE/ASEE Joint Propulsion Conference*, Atlanta, GA, July 2017, AIAA 2017-5045.